Mon. Not. R. Astron. Soc. **386,** 1252–1264 (2008) doi:10.1111/j.1365-2966.2008.13119.x

Properties of dusty tori in active galactic nuclei – I. The case of SWIRE/SDSS quasars

E. Hatziminaoglou,[1,2⋆] J. Fritz,[3] A. Franceschini,[3] A. Afonso-Luis,[2] A. Hernán-Caballero,[2] I. Pérez-Fournon,[2] S. Serjeant,[4] C. Lonsdale,[5,6] S. Oliver,[7] M. Rowan-Robinson,[8] D. Shupe,[5] H. E. Smith[9] and J. Surace[5]

[1]*European Southern Observatory, Karl-Schwarzschild-Str. 2, 85748 Garching bei München, Germany*
[2]*Instituto de Astrofísica de Canarias, C/Vía Láctea s/n, E-38200 La Laguna, Spain*
[3]*Dipartimento di Astronomia, Universita di Padova, Vicolo dell'Osservatorio 5, 35122 Padua, Italy*
[4]*Centre for Astrophysics and Planetary Science, School of Physical Sciences, University of Kent, Canterbury, Kent CT2 7NR*
[5]*Infrared Processing and Analysis Centre, California Institute of Technology, Pasadena, CA 91125, USA*
[6]*Department of Astronomy, University of Virginia, Charlottesville, VA 22904, USA*
[7]*Astronomy Centre, Department of Physics and Astronomy, University of Sussex, Falmer, Brighton BN1 9QJ*
[8]*Astrophysics Group, Blackett Laboratory, Imperial College London, London SW7 2BW*
[9]*Centre for Astrophysics and Space Sciences, University of California, San Diego, La Jolla, CA 92093-0424, USA*

Accepted 2008 February 15. Received 2008 February 8; in original form 2007 December 18

ABSTRACT

We derive the properties of dusty tori in active galactic nuclei from the comparison of observed spectral energy distributions (SEDs) of SDSS quasars and a precomputed grid of torus models. The observed SEDs comprise SDSS photometry, Two-Micron All-Sky Survey *J*, *H* and *K* data, whenever available, and mid-infrared (mid-IR) data from the Spitzer Wide-area InfraRed Extragalactic Survey. The adopted model is that of Fritz, Franceschini & Hatziminaoglou. The fit is performed by standard χ^2-minimization; the model, however, can be a multicomponent comprising a stellar and a starburst component, whenever necessary. Models with low equatorial optical depth, $\tau_{9.7}$, were allowed as well as 'traditional' models with $\tau_{9.7} \geqslant 1.0$, corresponding to $A_V \geqslant 22$ and the results were compared. Fits using high optical depth tori models only produced dust more compactly distributed than in the configuration where all $\tau_{9.7}$ models were permitted. Tori with decreasing dust density with the distance from the centre were favoured while there was no clear preference for models with or without angular variation of the dust density. The computed outer radii of the tori are of some tens of parsecs large but can reach, in a few cases, a few hundreds of parsecs. The mass of dust, $M_{\rm Dust}$, and IR luminosity, $L_{\rm IR}$, integrated in the wavelength range between 1 and 1000 μm, do not show significant variations with redshift, once the observational biases are taken into account. Objects with 70-μm detections, representing 25 per cent of the sample, are studied separately and the starburst contribution (whenever present) to the IR luminosity can reach, in the most extreme but very few cases, 80 per cent.

Key words: galaxies: active – quasars: general – galaxies: starburst – infrared: general.

1 INTRODUCTION

Efforts in understanding the physics at work in active galactic nuclei (AGN) started four decades ago. The origin of the infrared (IR) continuum of AGN was initially a matter of controversy, as it could be non-thermal but could equally be due to thermal emission from dust grains. It was long ago suggested (Rees et al. 1969) that IR emission radiation from Seyfert galaxies in the 2.2–22 μm wavelength range was produced by dust grains heated by ultraviolet (UV) and optical emission from the nucleus. Work carried out later on suggests the IR emission to be the reprocessed emission of the UV/optical radiation from the accretion disc by the particles composing the torus, namely silicate and graphite grains (e.g. Pier & Krolik 1992; Granato & Danese 1994; Efstathiou & Rowan-Robinson 1995; Nenkova, Ivezic & Elitzur 2002). Various configurations of the dust distribution geometry and compositions have been since suggested (e.g. Pier & Krolik 1992; van Bemmel & Dullemond 2003;

⋆E-mail: ehatzimi@eso.org

Dullemond & van Bemmel 2005; Elitzur & Shlosman 2006; Fritz et al. 2006).

Recent observations (Jaffe et al. 2004) indicate that this structure might be smaller than originally thought, but resolved in at least some nearby systems. Interferometric measurements at 8–13.5 μm centred on NGC 1068, a prototype Seyfert 2 galaxy, revealed a structure with an extent of ∼3.4 pc that can be identified with the torus (Jaffe et al. 2004).

Dust remains essential to understanding the Seyfert 1/2 dichotomy. The dust sublimation radius defines the outer boundary of the broad-line region (BLR). Recent results from reverberation mapping place the IR-emitting medium just beyond the BLR (Suganuma et al. 2006). The IR emitter presumably corresponds to the torus that would make a type 1 object look like a Seyfert 2 nucleus when the line-of-sight (LoS) to the BLR is obscured by the dusty medium. However, if the obscuring torus is 'clumpy' rather than homogeneous, as suggested by Krolik & Begelman (1988) and modelled by, for example, Nenkova et al. (2002), obscuration and classification of AGN becomes probabilistic.

In this paper, we address the question of the distribution of properties of dust tori around AGN, studying SDSS quasars in the fields covered by the Spitzer Wide-area InfraRed Extragalactic Survey (SWIRE[1]). We assume that tori are smooth (as opposed to 'clumpy') distributions of dust, composed of graphite and silicate grains and will limit ourselves to the use of photometry only, spanning a large wavelength range, from ∼0.35 to 160 μm. Our aim is to classify the properties of the objects under study fitting their observed spectral energy distributions (SEDs), built by photometric points collected from various surveys, to various model components, including stellar templates, AGN tori and starburst emission, whenever applicable. The quasar sample consists of all spectroscopically confirmed type 1 quasars in the common regions between SWIRE and SDSS Data Release 4 (DR4; Adelman-McCarthy et al. 2006). The purpose of this work is to constrain the model parameters and to quantify the IR properties of bright quasars, within the limitations imposed by the model assumptions, the resolution provided by the broad-band photometry, and the degeneracies resulting from the fitting procedure.

This paper is structured as follows. Section 2 describes in detail the samples. A brief description of the torus models and the stellar and starburst components is given in Section 3. Section 4 describes the SED fitting mechanism and the physical parameters thus derived. The results are presented in Section 5, with a subsection dedicated to the problems of degeneracy and aliasing and their implications. Finally, Section 6 presents a discussion of the results of this work.

2 THE SAMPLE

For the purposes of this study, consistent IR data are essential, covering as large a wavelength range as possible. SWIRE provided the astronomical community with unprecedented quality mid-infrared (mid-IR) photometric data for over 2 million objects, including hundreds of thousands of AGN of all types. We therefore selected the samples from regions with overlapping SDSS DR4 and SWIRE IRAC or MIPS 24-μm data; SWIRE ELAIS N1 and N2 and the Lockman field. The sample comprises 278 spectroscopically confirmed SDSS quasars within these fields with redshifts spanning $0.06 < z < 5.2$.

[1] http://swire.ipac.caltech.edu,lonsdale03

The SED of each object was constructed using the SDSS photometry (u, g, r, i, z), Two-Micron All-Sky Survey (2MASS) photometry (J, H, K) and IR photometry from SWIRE, that is, IRAC 1–4 channel fluxes, MIPS 24-, 70- and 160-μm fluxes, whenever available. 2MASS photometry from the 2MASS ×6 (Beichman et al. 2003) was used, for objects in the Lockman hole. The SWIRE catalogues we use throughout this work were processed by the SWIRE collaboration. Details about the data can be found in Lonsdale et al. (2004), Surace et al. (2004) and Shupe et al. (2008). The selection of 'reliable' sources in 70 and 160 μm is done as follows. All sources with detections above 5σ are considered reliable. The 70- and 160-μm flux limits adopted correspond to 90 per cent completeness and generally coincide with the 5σ noise of the images (measured from the sky rms). They slightly vary with the field, and for SWIRE ELAIS N1 and N2 and the Lockman fields they are of 17, 17.5 and 18 mJy for the 70 μm, and 104, 124 and 108 mJy for the 160 μm. Also sources with at least 3σ detections and a 24-μm counterpart brighter than 300 μJy, within 6 and 12 arcsec, for the 70- and 160-μm sources, are taken to be real. There will be, therefore, cases where the 70- and 160-μm fluxes will lie below the nominal flux limits. For more details, see Vaccari et al. (in preparation).

Richards et al. (2006) presented an extensive multiwavelength analysis of a sample of 259 objects, most of which belong to our quasar sample, also. For the colour properties and global SEDs, we therefore refer to this work. For a detailed analysis of the properties of the quasars and composite SEDs in SWIRE EN1 field, see also Hatziminaoglou et al. (2005).

Tables 1 and 2 list the coordinates, redshifts, optical, near- and mid-IR photometry of the 278 quasars. Here, only the first 20 entries are presented; the complete version of the tables is available as online material. The SWIRE fluxes missing from Table 2 do not indicate drop-outs but objects lying at the edges of the fields and escaped detection in some of the SWIRE bands due to slight variations in the rastering. As only a relatively small fraction of the sources have been detected in 70 μm, the 70- and 160-μm photometry will be presented in a separate table in Section 5.5.

3 THE MODEL COMPONENTS

The observed SED of a galaxy, from the UV to the far-IR (FIR), can in principle be built as the sum of three distinct components: stars, which emit most of their power in the optical, hot dust, heated by accretion on to a supermassive black hole, whose emission peaks in the mid-IR (from a few to some tens of μm) and cold dust, mainly heated by star formation.

3.1 The torus component

The main focus of this work is the dusty torus, for which we are seeking to determine the properties for the individual objects and for the sample as a whole. For the purposes of this work we assume a continuous dust distribution around the central sources (an accreting black hole), consisting of silicate and graphite grains, confined in a toroidal shape, as opposed to 'clumpy' tori models (see e.g. Nenkova et al. 2002). For a detailed description of the model, we refer to Fritz et al. (2006). Here, however, we summarize some of the major characteristics of the model.

The central source is assumed to be point-like and its emission isotropic. Its spectral energy distribution is defined by means of a composition of power laws [i.e. $\lambda L(\lambda) \propto \lambda^i$] with different values for the spectral index i. We adopted values found in the literature (e.g. Granato & Danese 1994; Schartmann et al. 2005), namely:

Table 1. Coordinates, redshifts and SDSS *ugriz* photometry for the first 20 quasars, ordered by RA.

Sequence number	RA	Dec.	z	u	g	r	i	z
1	10:30:39.62	+58:06:11.6	0.504	21.740 ± 0.17	20.392 ± 0.04	19.123 ± 0.02	18.158 ± 0.01	17.634 ± 0.02
2	10:30:58.68	+58:20:34.3	0.714	19.179 ± 0.02	18.992 ± 0.02	19.066 ± 0.01	19.121 ± 0.03	18.967 ± 0.06
3	10:31:13.74	+58:21:18.9	1.922	19.956 ± 0.03	19.955 ± 0.02	19.931 ± 0.02	19.723 ± 0.03	19.657 ± 0.10
4	10:31:20.11	+58:18:51.1	0.493	19.438 ± 0.03	19.136 ± 0.02	19.166 ± 0.01	18.892 ± 0.02	18.640 ± 0.03
5	10:31:47.64	+57:58:58.1	2.879	20.719 ± 0.07	19.418 ± 0.02	19.336 ± 0.02	19.267 ± 0.02	19.122 ± 0.04
6	10:31:57.06	+58:16:09.9	0.591	20.113 ± 0.04	19.735 ± 0.04	19.746 ± 0.02	19.408 ± 0.02	19.367 ± 0.05
7	10:32:22.85	+57:55:51.2	1.243	20.061 ± 0.04	20.187 ± 0.03	19.961 ± 0.03	20.044 ± 0.03	19.997 ± 0.08
8	10:32:27.93	+57:38:22.6	1.969	20.377 ± 0.05	20.416 ± 0.03	20.577 ± 0.03	20.371 ± 0.04	20.274 ± 0.10
9	10:32:36.21	+58:00:33.9	0.687	20.219 ± 0.04	19.854 ± 0.02	19.827 ± 0.02	19.637 ± 0.02	19.786 ± 0.07
10	10:32:53.03	+58:27:07.9	1.603	19.867 ± 0.04	19.787 ± 0.02	19.760 ± 0.02	19.569 ± 0.03	19.527 ± 0.09
11	10:33:01.52	+58:37:49.9	1.344	19.227 ± 0.02	19.177 ± 0.01	18.963 ± 0.01	19.131 ± 0.02	19.423 ± 0.08
12	10:33:20.31	+58:42:25.0	0.873	18.943 ± 0.02	18.897 ± 0.02	18.781 ± 0.01	18.790 ± 0.02	18.625 ± 0.04
13	10:33:33.93	+58:28:18.8	0.574	20.803 ± 0.07	20.306 ± 0.02	20.419 ± 0.03	20.218 ± 0.04	20.046 ± 0.14
14	10:33:52.75	+58:13:40.8	2.123	19.927 ± 0.05	19.863 ± 0.04	19.907 ± 0.02	19.799 ± 0.02	19.436 ± 0.06
15	10:33:59.97	+58:34:57.8	3.114	22.366 ± 0.36	19.835 ± 0.02	19.577 ± 0.02	19.486 ± 0.02	19.499 ± 0.08
16	10:34:13.89	+58:52:52.8	0.745	18.092 ± 0.01	17.807 ± 0.01	17.776 ± 0.01	17.825 ± 0.02	17.690 ± 0.02
17	10:34:21.24	+58:06:53.0	0.249	19.576 ± 0.07	18.965 ± 0.01	18.424 ± 0.01	18.106 ± 0.01	17.968 ± 0.05
18	10:34:25.70	+58:09:54.0	3.279	23.844 ± 0.94	20.241 ± 0.04	19.936 ± 0.02	19.831 ± 0.02	19.932 ± 0.08
19	10:35:08.02	+57:12:55.8	2.587	19.947 ± 0.04	19.666 ± 0.01	19.637 ± 0.02	19.639 ± 0.03	19.568 ± 0.06
20	10:35:17.52	+59:03:09.4	1.303	19.527 ± 0.03	19.656 ± 0.02	19.280 ± 0.02	19.316 ± 0.02	19.519 ± 0.09

Table 2. 2MASS photometry, IRAC (in μJy) and MIPS 24-μm fluxes (in mJy) for the first 20 quasars, ordered by RA.

Sequence number	J	H	K	$S_{3.6}$ (μJy)	$S_{4.5}$ (μJy)	$S_{5.8}$ (μJy)	$S_{8.0}$ (μJy)	S_{24} [mJy]
1	15.990 ± 0.02	14.945 ± 0.02	13.773 ± 0.01	5348.3 ± 6.89	6867.3 ± 5.97	9017.2 ± 20.88	11468.0 ± 11.24	–
2	–	–	–	390.04 ± 2.74	501.55 ± 3.03	–	981.08 ± 9.24	–
3	–	–	–	71.31 ± 0.84	106.62 ± 1.24	200.51 ± 4.37	306.49 ± 5.78	–
4	17.501 ± 0.07	16.529 ± 0.09	15.776 ± 0.07	589.85 ± 2.39	688.12 ± 2.18	864.29 ± 7.74	985.89 ± 5.82	–
5	–	–	–	100.28 ± 1.07	115.14 ± 1.15	167.05 ± 5.19	298.72 ± 5.19	1.019 ± 0.01
6	–	–	–	227.3 ± 1.24	290.32 ± 1.38	414.32 ± 5.1	565.18 ± 4.97	2.534 ± 0.03
7	–	–	–	116.49 ± 0.93	158.44 ± 1.42	204.23 ± 4.41	284.76 ± 5.78	0.612 ± 0.01
8	–	–	–	58.28 ± 1.66	–	162.75 ± 8.58	–	0.490 ± 0.01
9	–	–	–	171.56 ± 1.0	245.13 ± 1.36	345.04 ± 4.61	475.43 ± 4.95	1.165 ± 0.01
10	–	–	–	95.53 ± 1.09	142.35 ± 1.35	198.96 ± 5.38	359.6 ± 5.91	0.877 ± 0.03
11	–	–	–	273.12 ± 2.26	419.03 ± 2.97	592.55 ± 8.17	857.97 ± 7.6	–
12	17.505 ± 0.09	17.070 ± 0.16	16.437 ± 0.16	548.98 ± 4.46	590.21 ± 3.36	922.55 ± 15.01	1163.0 ± 7.53	–
13	–	–	–	168.42 ± 1.5	187.89 ± 2.07	221.55 ± 5.31	239.63 ± 5.96	0.741 ± 0.01
14	–	–	–	73.37 ± 0.78	91.090 ± 0.97	151.93 ± 3.48	224.17 ± 4.65	0.576 ± 0.01
15	–	–	–	65.22 ± 1.17	84.420 ± 1.25	148.57 ± 6.01	286.36 ± 5.0	1.050 ± 0.01
16	16.603 ± 0.04	16.132 ± 0.08	15.374 ± 0.07	1331.7 ± 6.95	1987.1 ± 7.65	2734.3 ± 24.62	4106.1 ± 16.07	–
17	17.114 ± 0.07	16.323 ± 0.09	15.688 ± 0.09	356.5 ± 2.23	422.01 ± 2.56	458.92 ± 7.61	1147.9 ± 6.85	3.309 ± 0.01
18	–	–	–	51.74 ± 0.71	60.800 ± 1.08	72.440 ± 3.95	128.3 ± 5.58	0.511 ± 0.01
19	–	–	–	–	–	–	–	0.621 ± 0.01
20	–	–	–	204.23 ± 2.79	326.77 ± 3.73	412.04 ± 11.06	634.96 ± 9.99	–

$i = 1.2$ for $0.001 < \lambda < 0.03$, $i = 0$ for $0.03 < \lambda < 0.125$, $i = -0.5$ and $i = -1.0$ for $0.125 < \lambda < 10$, and a Rayleigh–Jeans decline ($i = -3.0$) is assumed longward of $\lambda = 10$, where λ is given in μm.

The torus geometry adopted to describe the shape and the spatial distribution of dust is the so-called 'flared disc' (see e.g. Efstathiou & Rowan-Robinson 1995; Manske, Henning & Men'shchikov 1998; van Bemmel & Dullemond 2003) that is a sphere with the polar cones removed. Its size is defined by its outer radius, $R_{\rm out}$, and the opening angle, Θ, of the torus itself. The dust components that dominate both the absorption and the emission of radiation are graphite and silicate. The location of the inner radius, $R_{\rm in}$, depends both on the sublimation temperature of the dust grains [1500 and 1000 K, for graphite (Barvainis 1987) and silicate (Granato & Danese 1994), respectively] and on the strength of the accretion luminosity. We adopted the absorption and scattering coefficients given by Laor & Draine (1993) for dust grains of different dimensions, weighted with the standard MRN distribution (Mathis, Rumpl & Nordsieck 1977). Grains dimensions range from 0.005 to 0.25 μm for graphite, and 0.025 to 0.25 μm for silicate.

The dust density within the torus is modelled in such a way to allow a gradient along both the radial and the angular coordinates:

$$\rho(r, \theta) = \alpha\, r^{\beta}\, {\rm e}^{-\gamma |\cos(\theta)|} \quad (1)$$

with β taking the discrete values 0.0, −0.5 and −1.0, and γ the values 0.0 and 6.0. When $\gamma \neq 0.0$ the dust distribution in no longer a 'flared disc' but takes a shape that resembles that of a donut, hence

the name 'torus'. The 'zero value' α is defined by the value of the equatorial optical depth at 9.7 μm, $\tau_{9.7}$. One of the novelties of this work is the use of low optical depth tori ($\tau_{9.7} < 1$). Even though they are part of model sets present in the literature (e.g. Granato & Danese 1994), they have not been used to explain the IR emission of AGN. The implications of this approach are explained in Section 6.

The global model SEDs are computed at different angles of the LoS with respect to the torus equatorial plane, in order to account for both type 1 and type 2 objects emission, and include three contributions: emission from the AGN (partially extinguished if the torus intercepts the LoS), thermal and scattering emission by dust in each volume element.

Torus models with $R_{\rm out}/R_{\rm in}$ of 300 are a priori excluded from the runs, even though they belong to the 'standard' grid of models presented by Fritz et al. (2006), as they imply tori with physical sizes of several hundred parsecs, sometimes even kpc. For such a ratio, an AGN of 10^{46} erg s^{-1} accretion luminosity and an inner radius of 1.3 pc would have an outer radius of ∼400 pc. In the general case, only models with $R_{\rm out}/R_{\rm in}$ of 30 and 100 are allowed, but models with $R_{\rm out}/R_{\rm in}$ of 300 will be revisited in Section 5.5 in order to address specific cases.

3.2 The stellar component

The stellar emission will play a minor role in this work, since we are dealing with bright, mainly high-redshift quasars, for which the galaxy light is not significant. However, for completeness, we add a stellar component modelled as the sum of spectra of simple stellar population (SSP) models of different age, all assumed with a common (solar) metallicity. The set of SSP used for this analysis is built with Padova evolutionary tracks (Bertelli et al. 1994), a Salpeter initial mass function with masses in the range 0.15–120 $M_\odot$ and the Jacoby, Hunter & Christian (1984) library of observed stellar spectra in the optical domain. The extension to the UV and IR range is obtained by means of Kurucz theoretical libraries. Dust emission from circumstellar envelopes of AGB stars has been added by Bressan, Granato & Silva (1998).

3.3 The starburst component

For the cold dust component, the major contributor to the emission at wavelengths longer than ∼30μm, we use two observational starburst templates, namely M82 as a representative of a 'typical' starburst IR emission and Arp 220 as representative of a very extinguished starburst. A more exhaustive approach would require us to provide a physical model of the starburst component, which however is far beyond the scope of this work. Starburst templates are used only when there are observed data points longward of 24-μm rest frame (typically only when 70- and/or 160-μm data are available), and if a torus model fails to provide an acceptable description of the observational SED.

This choice is, in fact, arbitrary as nothing forbids the presence of a starburst component fainter than the 70-μm detection limit. The flux at 24 μm, though, is dominated by the torus: the starburst contribution at this wavelength is minimal, as it coincides with the presence of a deep absorption feature in their SEDs (see Section 5.5), an with no more data points redwards of 24 μm it is simply impossible to constrain that part of the SED. Adding a starburst component in order to fit all objects would only increase the degeneracy and uncertainties of our results. Quantities such as the IR luminosity (see Sections 4.1 and 5.2), though, might be seen as lower limits for the objects with no MIPS 70- and/or 160-μm detections.

4 SED FITTING

Given the large amount of data available, we developed a fully automatic fitting procedure, where the goodness of the fit is measured in terms of a χ^2 function:

$$\chi^2 = \sum_i^N \left(\frac{O_i - M_i}{\sigma_i} \right)^2 \quad (2)$$

where O_i are the observed values, M_i the values computed from the model and σ_i are the observed errors of the ith photometric point. The expected values from the model are computed by convolving the synthetic flux with the filters' response curves, after an opportune normalization and K-correction is applied. The dominant component in the UV and near-infrared (near-IR) (rest frame) is the accretion disc. For very low redshift objects light from the host galaxy might also be present. The former is clearly distinguishable from a typical stellar SED, because it is in general bluer and flat over the entire range of overlap. Hence, if a good fit is not achieved, stars are removed from the final SED, and a pure AGN component is used at these wavelengths. Since we are dealing with an AGN sample (i.e. we expect an AGN component to be present in the observed SEDs of all the objects), the starburst emission, which dominates over the other components only in the FIR, is included only if there are observed 70- and/or 160-μm data points.

Examples of fits are shown in Fig. 1: on the left-hand panel, an object whose SED was reproduced by an AGN component only; in the middle panel a case of an AGN with starburst emission; and in the right-hand panel an object with all three components (torus, starburst and stars) present.

Even though the minimum χ^2 will define the best fit, the associated probabilities can not be taken at face value, as for a number of reasons the derived reduced values of χ^2 are overestimated. First of all, in order to compute the model magnitudes, the models are convolved with the filters' transmission curves. If the model is a very accurate representation of the real SED of an object, this convolution will lead to more accurate results. In our case, however, the optical/UV part of the model is simply a power law, as already mentioned in Section 3.1, while the SDSS photometry that corresponds to the same part of the SED is quite sensitive to the presence of broad emission lines or the presence of the small blue bump.[2] Also, as a general remark, the photometric errors are very small (typically of the order of few percent, as seen in Tables 1 and 2) for both SDSS and SWIRE data points. And even though we use the errors in the catalogues to properly weight the fits, in many cases the computed values of the reduced values of χ^2 are very high due to the small photometric errors. In order to avoid excessively high weighting and high χ^2 values, many SED fitting codes impose minimum flux errors (e.g. HyperZ, Bolzonella, Miralles & Pelló 2000; ImpZ, Babbedge et al. 2004); here, however, we chose not to adopt this approach.

4.1 From SED fitting to physical parameters

Based on the best-fitting model parameters, a number of other physical parameters can be derived.

[2] The optical/UV continuum, however, is very well constrained by the available data points and therefore the computation of the accretion luminosity is not affected – see also Section 4.1.

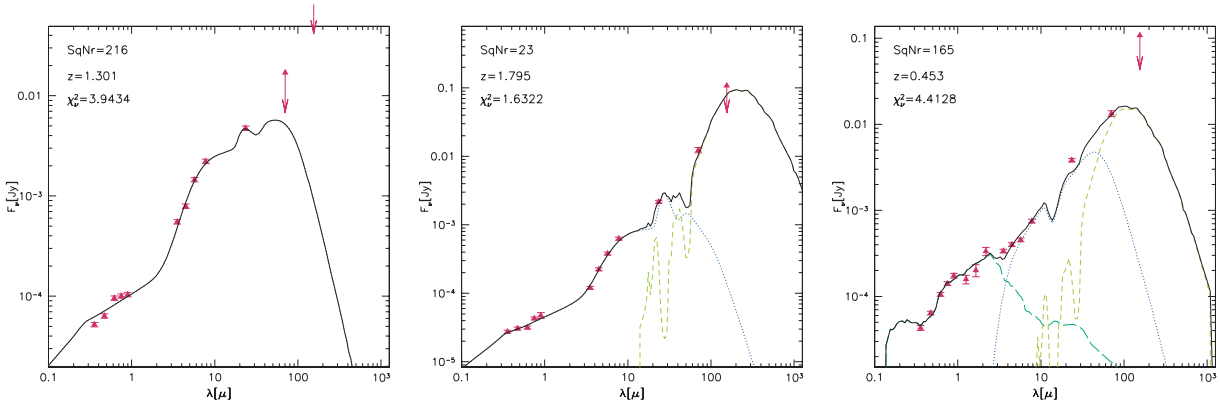

Figure 1. Examples of fits: an object whose SED was reproduced by an AGN component only (left-hand panel); a case of an AGN with starburst emission (middle panel); and an object with all three components (torus, starburst and stars) present (right-hand panel).

(i) *The accretion luminosity*, $L_{\rm acc}$. This is, the soft X-ray, UV and optical luminosity coming from the accretion disc, which provides the main source of dust heating in the torus.

(ii) *The IR luminosity*, $L_{\rm IR}$. It is defined as the integral of all the components in the interval 1–1000 μm.

(iii) *The relative contribution to the IR.* The relative contribution of AGN and starburst activity to the IR luminosity (the latter is computed only where 70- and/or 160-μm data are available), that is, the fraction of each component with respect to the total IR luminosity.

(iv) *The innermost radius of the torus*, $R_{\rm in}$. It is the distance at which the grains reach their sublimation temperature, averaged over all sizes of graphite grains:

$$R_{\rm in} \simeq 1.3 \sqrt{L_{\rm acc}}\, T_{1500}^{-2.8} \qquad ({\rm pc}), \tag{3}$$

where T_{1500} is the sublimation temperature of the dust grain given in units of 1500 K (Barvainis 1987).

(v) *The optical depth.* The optical depth (or extinction in the V band) along the LoS.

(vi) *The hydrogen column density.* The hydrogen column density along the LoS (note that in this case the Galactic dust-to-gas ratio is implicitly assumed as a consequence of the use of the MRN distribution function).

(vii) *The torus full opening angle.* This parameter also defines the covering factor (CF), which is the percentage of the solid angle which is covered by dust in the torus, as seen from the nucleus.

(viii) *The mass of dust*, $\rm M_{Dust}$. Within the torus, it is the integral of all dust grains over all volume elements.

4.2 High and low optical depth, $\tau_{9.7}$, models

We also address the issue of low optical depth tori, namely tori with equatorial $\tau_{9.7} \leqslant 1.0$, equivalent to $A_V \leqslant 22$. The obscuring medium (torus) is usually considered to be optically thick but there are no physical arguments against the existence of optically thin tori. We therefore test the possibility of quasars seen also through low optical depth tori, as opposed to the 'traditional' picture of them seen uniquely on lines of sight not intercept by the torus. In order to do so, we run the SED fitting twice, once allowing for all optical depths, and once allowing only for models with ($\tau_{9.7} \geqslant 1.0$), and compared the results.

5 RESULTS

From the 278 quasars comprising the sample, 247 have IRAC coverage, 86 of which have additional *JHK* data from 2MASS (of a total of 97 quasars of our sample detected by 2MASS) and a total of 268 has a 24-μm data point. If one requires a good sampling of the SEDs, one might require detections in at least eight bands: u, g, r, i, z, two out of four IRAC bands (due to slight differences in the rastering, objects that lie at the edges of the fields might escape detection in 2 of the 4 bands) and MIPS 24 μm. Similar considerations apply in that the objects that were not detected in this band were not dropouts but simply happened to lie outside the covered areas. This condition is fulfilled by 237 out of the 278 objects. For 70 of these, there are 70-μm detections. The 41 objects that do not have IRAC data or 24-μm detections were included in the sample but it will be made clear whenever their exclusion causes changes in the results mentioned below.

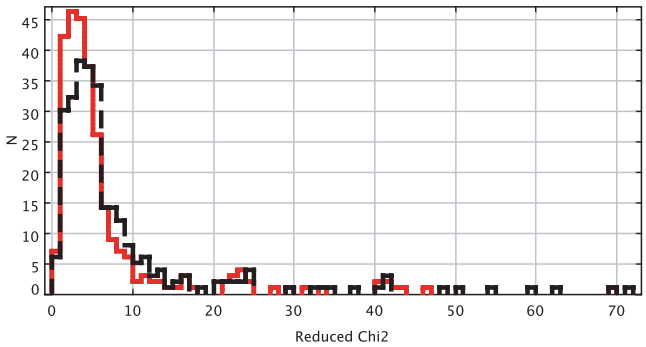

Figure 2. Minimum χ^2-distribution in the case all models are allowed in the fits (red plain line) and that of only high-$\tau_{9.7}$ torus models allowed (black dashed line).

Fig. 2 shows the minimum χ^2 distribution in the case all models are allowed in the fits (red plain line) and that of only high-$\tau_{9.7}$ torus models allowed (black dashed line). For the statistical analysis of the sample and based on the discussion presented in Section 4, we consider the objects for which the best-fitting solutions have reduced χ^2 lower than 16 for both runs. This cut is of course arbitrary and it has been chosen because it corresponds to a minimum in the χ^2 distribution corresponding to the run where all $\tau_{9.7}$ where allowed (see Fig. 2). This cut will exclude in both runs 10 per cent of the objects. Note that the χ^2 is narrower in the case where all models are allowed, but broadens when constraints on the model grid are imposed. Having chosen a more conservative cut in the values of reduced χ^2, for example, 10, would have excluded another ∼4 per cent of the fits and would not further affect the results.

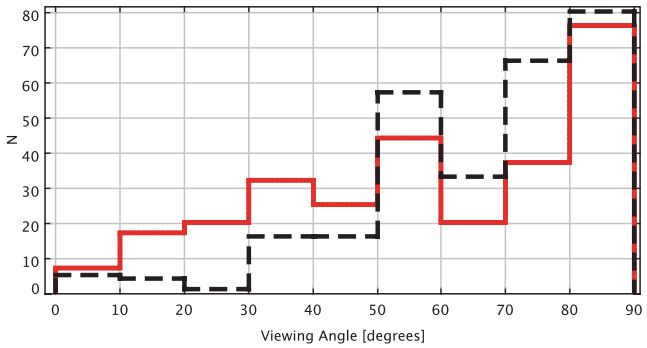

Figure 3. Distribution of viewing angle (in °), from the equatorial plane. The red solid line (black dashed line) corresponds to the run with all torus models allowed (only high equatorial optical depth, $\tau_{9.7}$, models allowed).

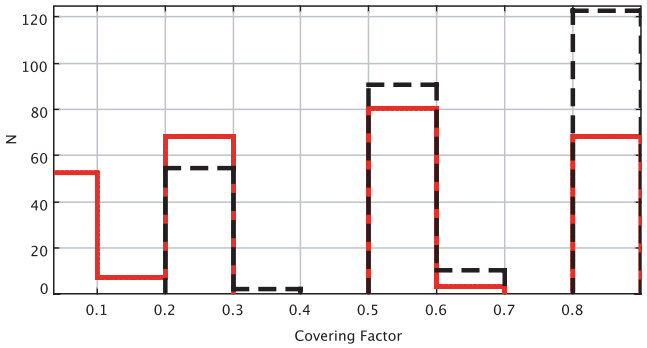

Figure 4. Distribution of the best-fitting values for the torus CF. Colour-coding is the same as for Figs 2 and 3. The gaps are due to the discrete values given to the torus half-opening angle when the grid of models was built (see the text for more details).

From the 250 of the 278 with reduced $\chi^2 < 16$, 190 were better matched with an AGN component alone, 46 required an additional starburst component, five more were sets of AGN, starburst and stellar component, and another nine were just composed of stars and an AGN.

Tori with β equal to -1.0, were slightly favoured, with 40 per cent of the observed SEDs being reproduced by such models, with $\beta = -0.5$ and 0.0 providing better fits to 32 and 28 per cent of the objects, respectively. Models with γ equal to 6.0 (see equation 1) provided better fits to 46 per cent of the sample while there was a slight tendency towards tori with $R_{\rm out}/R_{\rm in}$ of 100 (59 per cent of the objects). However, when high $\tau_{9.7}$ were forced to the fit, the tendencies were reversed, with 56 per cent of the objects favouring models with γ equal to 6.0 and $R_{\rm out}/R_{\rm in}$ of 30 and 50 per cent of the objects better matching $\beta = -1.0$. All these changes tend to produce dust more compactly distributed than in the configuration where all $\tau_{9.7}$ models were permitted and this change occurred most probably in order to avoid large amounts of IR emission to be produced otherwise by the model.

Fig. 3 shows the distribution of the best values for the viewing angles, measured from the equatorial plane towards the pole, for objects with minimum values of χ^2 below the selected threshold. The colour coding is the same as in Fig. 2.

When all optical depths are allowed, the SEDs of more objects could be reproduced with configurations allowing for the LoS to intercept a (low $\tau_{9.7}$) torus. When only high $\tau_{9.7}$ values are allowed, the histogram of viewing angles is depleted towards the low angles end and boosted towards the large angles end, as expected from our current view of the AGN paradigm, in which type 1 objects can not be seen through the torus. In both cases, however, for the majority of objects the viewing angle is larger than half the torus effective angle, and therefore the LoS does not intercept it.

5.1 The covering factor

The CF, as already mentioned, is the percentage of the solid angle blocking the light of the AGN due to dust absorption. For models with high equatorial optical depths, $\tau_{9.7}$, it is proportional to the cosine of the effective opening angle of the torus. Fig. 4 shows the distribution of CF for the run with all models allowed and that for which only high values of $\tau_{9.7}$ were used. The gaps are due to the discrete values given to the torus half opening angle when the grid of models was built, namely of 20°, 40° and 60°. For low-$\tau_{9.7}$ models and models with density decreasing towards high altitudes above the equatorial plane ($\gamma > 0$ in equation 1) though, the CF has to be recomputed to account for the fact that the torus obscuration is considered effective only where $\tau(\lambda = 0.3\ \mu) > 1$.

The colour coding is the same as that in Fig. 2. The plot implies that very low optical depth tori correspond to very small CFs (first bin of red solid histogram). This happens because in these cases the CF is recomputed to account for the fact that the quasars could be seen through an optically very thin medium. We consider that the LoS intercepts the torus when the optical depth at 3000 Å reaches the value of 1. When these models are excluded, the CF assumes a steeper distribution, with many more objects having much larger dust coverage.

5.2 IR luminosity and mass of dust

For objects whose mid-IR SED can be represented by a torus component only, the ratio of $L_{\rm acc}$ over the IR luminosity, $L_{\rm IR}$, would be another indicator of the obscuration. IR radiation is UV/optical radiation reprocessed by the dust composing the torus. For type 1 objects, for which the central engine is directly observed, this ratio is expected to take values larger than unity, as indeed is the case. Furthermore, $L_{\rm acc}/L_{\rm IR}$ does not show any dependence neither on redshift nor on $L_{\rm acc}$. There is, however, a clear tendency of decreasing $L_{\rm acc}/L_{\rm IR}$ with increasing viewing angle shown in Fig. 5, with a factor of 4 of difference between 10° and 90°. This tendency is due to the

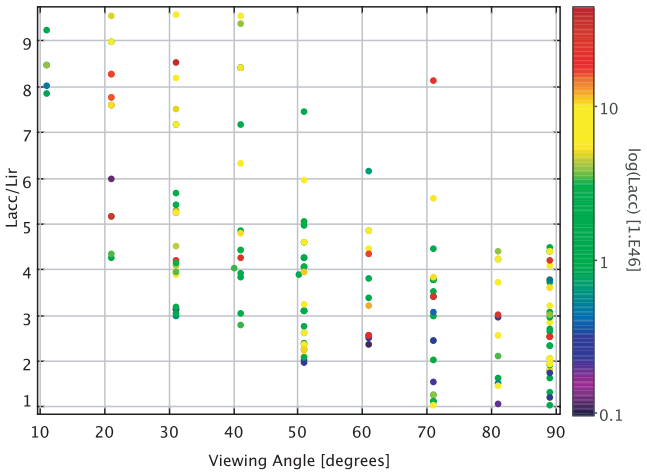

Figure 5. $L_{\rm acc}/L_{\rm IR}$ as a function of the viewing angle and the accretion luminosity, $L_{\rm acc}$.

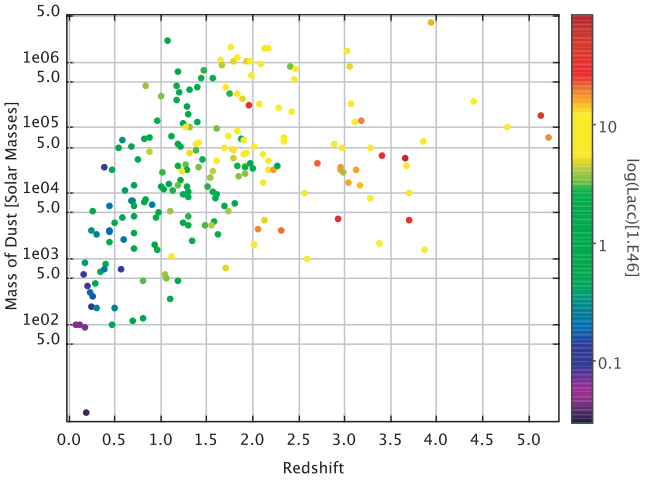

Figure 6. Mass of dust, $M_{\rm Dust}$, as a function of redshift, z, and accretion luminosity, $L_{\rm acc}$.

fact that $L_{\rm IR}$ is orientation-independent while the measurements of $L_{\rm acc}$ are not, translated into a constant $L_{\rm IR}$ and a *decreasing* $L_{\rm acc}$ with increasing viewing angle. From the results of the best-fitting models one notes that objects with best viewing angles of less than 30°, are also assigned models with an angular variation of the dust density, that is, $\gamma = -6.0$. The ratio of $\gamma(-6.0)/\gamma(0.0)$ drops to 0.85 for objects with best viewing angles between 40° and 60° and to 0.5 for objects seen from even higher viewing angles. The objects with $\gamma = -6.0$ tend to have, on average, larger accretion luminosities suggesting that $L_{\rm acc}$ might be influencing the dust distribution as well as the torus opening angle.

$L_{\rm IR}$ also increases with increasing $M_{\rm Dust}$, as larger amounts of dust produce stronger IR emission. The mass of dust, $M_{\rm Dust}$, increases with redshift as well as with $L_{\rm acc}$ (Fig. 6). The dependence on the redshift, however, is mainly an observational bias: $M_{\rm Dust}$ is computed integrating over all dust grains over all volume elements of the torus and therefore depends on $R_{\rm in}$ that scales with $\sqrt{(L_{\rm acc})}$ (from equation 3), which increases with increasing redshift (Scott effect).

In order to make sure that all tendencies with redshifts are simply the result of the observational bias all flux-limited samples suffer from, we divided part of the sample to slices of $L_{\rm acc}$ and redshift and computed the mean for $M_{\rm Dust}$, $L_{\rm IR}$ and CF in these bins. The bins were chosen in a way to have at least 3 redshift ones per luminosity range. The result are given in Table 3. The three quantities show no statistically significant trend with redshift in either of the two $L_{\rm acc}$ bins. The average values of the three quantities show an increase in lower luminosity bin but can be considered constant within the errors.

The results on the accretion luminosity and the dust mass are independent of the choice to impose high optical depth models in the fits. The distributions shown in Fig. 5 are indistinguishable. This confirms the robustness of the derived values of $L_{\rm acc}$, as further discussed in Section 5.6.

5.3 The torus dimensions

The inner radius of the torus, that is, the minimum distance at which dust grains can exist, is computed from equation 3 and for the sample under study typically takes values up to 5 pc, with a broad distribution and a peak at ∼2 pc. Equation (3), however, only takes into account the accretion luminosity as a heating source for the dust. And while this is realistic for the majority of cases, there are some particular conditions, for which the thermal emission from dust itself can become an important, non-negligible contributor to its self-heating. This this likely to occur in models with steep density profiles ($\beta \leqslant -1$) and high optical depths that will give rise to so high density at the inner radius that a large amount of the dust-emitted radiation is re-absorbed locally and the sublimation temperature is reached and exceeded for all the dust grains. When this happens during the computation of a model, the inner radius is moved to larger values, at steps of 0.2 pc, and the calculation of the equilibrium temperature starts again. This procedure is repeated until the temperature at the innermost radius remains below the sublimation value.

As already mentioned, our models use a fixed $R_{\rm out}/R_{\rm in}$ ratio, namely of 30 and 100. These cuts are only useful when the dust density is assumed constant and does not vary neither with the distance to the centre nor with the angle from the equatorial plane, that is, when $\beta = 0.0$ and $\gamma = 0.0$. When $\beta = -1.0$ though, the dust density rapidly decreases with the distance to the centre and the value of $R_{\rm out}$ is in practice much smaller than that given by the constant $R_{\rm out}/R_{\rm in}$ ratios. We find the outer radii of the tori to be typically some tens of parsecs large but can reach, in a few cases, a few hundreds of parsecs.

5.4 Equatorial optical depth and hydrogen column density, $N_{\rm H}$

The hydrogen column density, $N_{\rm H}$, is proportional to the optical depth and is defined as (Fritz et al. 2006):

$$\tau_{\rm eq}(\lambda) = N_{\rm H} \times \sum_{id=1}^{N_{\rm dust}} \left[Q^{A}_{id}(\lambda) + Q^{S}_{id}(\lambda) \right] a^{2}_{id} \pi N d_{id}, \quad (4)$$

where $Q^{\rm A}_{id}$ and $Q^{\rm S}_{id}$ are the absorption and scattering coefficients, of the idth dust grain, respectively, $N_{\rm tot}$ is the total number of grain sizes, a_{id} their radius and N_{id} is the number of grain, of a given dimension, calculated with respect to hydrogen. The equatorial optical depth, $\tau_{\rm eq}$, is in general different of that computed along the LoS.

Fig. 7 shows that high $\tau_{9.7}$ models correspond to very high equatorial hydrogen column densities, $N_{\rm H}$, while allowing for low $\tau_{9.7}$

Table 3. $M_{\rm Dust}$, $L_{\rm IR}$ and CF averaged over redshift and luminosity bins.

Bin #	N	$L_{\rm acc}$ (10^{46} erg s^{-1})	z	$M_{\rm Dust}$ ($M_\odot$)	$L_{\rm IR}$ (10^{46} erg s^{-1})	CF
1	8	2.0–5.0	0.5–1.0	0.66 ± 1.34	0.96 ± 0.35	0.42 ± 0.34
2	37	2.0–5.0	1.0–1.5	1.22 ± 1.75	1.13 ± 0.91	0.43 ± 0.27
3	27	2.0–5.0	1.5–2.0	1.75 ± 2.99	1.25 ± 0.71	0.49 ± 0.27
4	7	5.0–10.0	1.0–1.5	2.59 ± 3.95	1.97 ± 1.61	0.31 ± 0.19
5	18	5.0–10.0	1.5–2.0	3.88 ± 4.83	2.90 ± 2.02	0.52 ± 0.26
6	14	5.0–10.0	2.0–2.5	2.84 ± 4.50	2.44 ± 1.24	0.45 ± 0.28

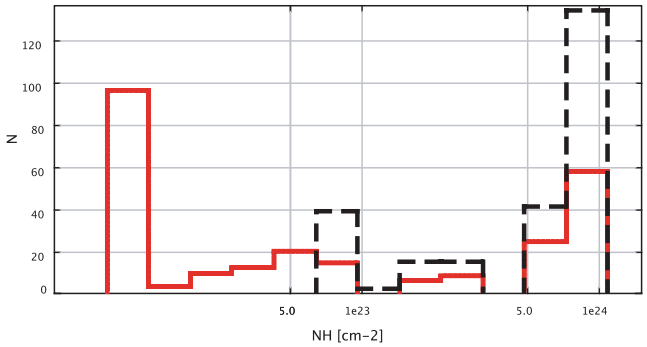

Figure 7. Equatorial hydrogen column density, $N_{\rm H}$, distribution for all models (red plain line) and high optical depth models (black dashed line).

values of $N_{\rm H}$ as low as a few times 10^{21} are feasible. In the latter case, the $N_{\rm H}$ distribution is bimodal peaking at the extreme of the values allowed.

The $N_{\rm H}$ values as derived from the model may not be directly comparable to observed ones (e.g. those computed via X-ray observations). In this study, we assume a Galactic dust-to-gas ratio that is likely to vary from one galaxy to another. Furthermore, the model value is only accounting for hydrogen within the torus, while observations one takes into account also the gas within the torus inner radius, as well as the gas likely present in the outer parts of the galaxy as, for example, diffuse medium.

5.5 The objects with 70- and 160-μm detections

The objects with 70-μm detection represent 25 per cent of the sample under study. They have already been included in our previous analysis but are worth a closer scrutiny. Their 70- and 160-μm fluxes, as well as their properties, derived from the best-fitting models are shown in Table 4. The distribution of their F_{70}/F_{24} colour versus their 24-μm fluxes, F_{24}, is shown in Fig. 8. F_{70}/F_{24} usually takes values in the range between 1 and 8, even for the brightest 24 μm sources, depending on the relative contribution of the starburst to the IR luminosity. For objects with $F_{24} \leqslant 0.3$ mJy there are no 70-μm detections because of the 70 μm limiting flux of the survey and the 70 μm source definition (see Section 2).

Out of the 70 objects, 55 had acceptable fits (with $\chi^2 \leqslant 16$), with only one detected at 160 μm. Five of the 55 observed SEDs were reproduced with a single component only, namely a torus; the other 50 required a starburst template. Five low redshift objects also required a stellar population to fit the optical/UV part of their SEDs. As mentioned in Section 3.3 two starburst templates were used in the fits, Arp220 and M82. Figs 9 and 10 show the observed SEDs (red triangles) and the components of the models reproducing them for the 55 objects with good reduced χ^2 and an assigned starburst. The torus components are shown in the blue dotted lines, the starbursts in the light green dashed lines and the stellar components in the dark green long-dashed lines. The total models are illustrated in the solid black lines.

All but one objects were assigned an Arp220-like template to reproduce their 70-μm detection. The reason for that is the very bright limiting magnitude of the survey in the MIPS Ge bands. An Arp220-like component could make the 70-μm detection bright enough to be observed without contributing to the IRAC fluxes while an M82 component would also contribute considerably to the IRAC and MIPS 24-μm fluxes.

Another point favouring the conclusion that objects not detected at 70 μm could in fact be characterized by a less extreme starburst (e.g. M82-like) starburst is the fact that even though objects with 70-μm detections are the brightest at 24 μm, not all bright 24 μm sources have a 70-μm detection, as seen in Fig. 11. The opposite, that is, all bright 24-μm sources observed at 70 μm, would imply that fainter 24 μm sources would have different F_{70}/F_{24} ratios and therefore a different starburst component (M82), but there is no observational evidence in favour.

The contributions of the AGN to the total IR luminosity, as defined in Section 4.1, for the objects with starburst components is shown in Fig. 12 (filled circles for the run with all $\tau_{9.7}$, open circles for the run with high values of $\tau_{9.7}$), as a function of their 24-μm flux and redshift. The mean difference of the AGN contribution derived from the two runs is of 3 per cent with a standard deviation of 8 per cent, the results can therefore be considered independent of the choice of values of $\tau_{9.7}$. The AGN fraction varies from ∼20 per cent up to 100 per cent, with lower redshift objects tending to have higher AGN contribution. The increase of the AGN fraction with the 24-μm flux is due to the fact that, when the starburst component is an Arp220, the 24-μm flux is produced by the torus alone, as it corresponds to a very deep absorption feature in the starburst template. This requires a brighter AGN and a lower starburst component in order to keep the ratio F_{70}/F_{24} in the observed range. The presence of strong starburst component in many of the cases is an interesting result, when one considers the fact that the quasars under study are among the brightest in the sky.

It could be argued that allowing for larger dust distributions might increase the fraction of the AGN contribution to the IR luminosity or reproduce the 70-μm point without the need of a starburst component. In order to account for this possibility but also in an effort to reproduce the few observed 160-μm data points and potentially improve the fit for the rest of the objects with 70-μm data, we re-run the SED fitting allowing for models with $R_{\rm out}/R_{\rm in} = 300$, a priori excluded from the runs for reasons presented in Section 3.1. In none of the cases, however, was a torus component alone enough to reproduce the 70-μm point. In fact, all objects required a starburst component (again Arp220) with a contribution within at most 10 per cent lower than that predicted when no large tori were allowed. Furthermore, the 160-μm points were still not properly reproduced, as all combinations of torus and starburst templates produced model SEDs lying significantly below the observed 160-μm points.

5.6 Multiple local minimae and degeneracy

SED fitting in a multi-parameter space usually involves degeneracies, that is, the existence of various combinations of parameter values that yield equally good results when reproducing a set of observed data points. Here we are focusing on the properties of the AGN emission, and we will hence not face this issue with respect to the stellar component (both stars and dust heated by star formation). We will exploit the fact that the mid-IR domain is strongly dominated by AGN in our sample objects. With respect to this approach, the degeneracy problem translates into the fact that there are more AGN models, with different parameters that yield equally good – or acceptable in terms of χ^2 values – fits, so that the properties of the dusty torus can not be unequivocally assessed.

To properly deal with this issue, we keep trace of the exploration of the model's parameter space, and we analyse the 30 best model fits for each object of the sample. For most of the objects, even when only the first two solutions are considered the discrepancies, measured as Δparam/param(0) where param(0) is the value of a

Table 4. Coordinates, redshift, 70- and 160-μm fluxes, starburst template used in the best fit and AGN fraction with respect to the IR luminosity for the 70 objects with 70-μm detections, ordered by RA.

Sequence number	RA	Dec.	z	S_{70} (mJy)	S_{160} (mJy)	SB	AGN_{frac}
17	10:34:21.24	+58:06:53.0	0.249	18.71 ± 1.33	–	Arp220	0.3939
23	10:35:52.62	+58:43:25.8	1.795	12.35 ± 1.13	–	Arp220	0.2059
29	10:36:51.94	+57:59:51.0	0.5	24.12 ± 1.2	–	Arp220	0.5809
33	10:37:24.74	+58:05:13.1	1.517	19.68 ± 0.95	–	Arp220	0.5406
37	10:38:03.35	+57:27:01.7	1.285	80.51 ± 1.53	130.25 ± 5.0	Arp220	0.319
52	10:40:49.10	+59:06:24.4	1.588	11.69 ± 0.83	–	Arp220	0.1908
53	10:40:58.80	+58:17:03.3	0.071	17.04 ± 0.93	–	Arp220	0.723
60	10:41:19.23	+57:45:00.1	0.067	705.5 ± 6.94	642.91 ± 6.61	M82	0.0015
65	10:41:55.16	+57:16:03.3	1.721	25.44 ± 1.1	–	Arp220	0.2639
72	10:42:55.65	+57:55:49.9	1.468	19.55 ± 0.92	–	Arp220	0.5584
89	10:45:26.72	+59:54:22.5	0.646	13.92 ± 1.19	–	Arp220	0.6861
90	10:45:39.27	+58:07:11.1	1.149	19.55 ± 1.27	–	Arp220	0.2901
96	10:46:22.61	+57:40:34.2	1.343	15.11 ± 1.15	–	Arp220	0.5129
103	10:47:05.57	+58:27:41.8	0.244	9.699 ± 0.73	–	Arp220	0.3954
108	10:47:39.50	+56:35:07.2	0.303	59.04 ± 1.13	376.88 ± 0.01	Arp220	0.2771
110	10:47:56.98	+56:24:47.2	0.166	36.72 ± 1.38	–	Arp220	0.2677
111	10:47:57.52	+57:34:51.8	1.102	10.39 ± 0.89	–	Arp220	0.478
112	10:48:06.19	+56:30:21.5	1.905	10.55 ± 1.44	–	Arp220	0.3462
113	10:48:09.18	+57:02:42.0	3.249	13.19 ± 0.92	47.83 ± 4.5	Arp220	0.3071
123	10:49:25.88	+57:54:21.6	0.071	21.00 ± 1.05	–	Arp220	0.8394
125	10:49:30.46	+59:20:32.6	1.011	17.76 ± 0.95	–	Arp220	0.5055
138	10:51:06.12	+59:16:25.2	0.768	27.47 ± 0.93	–	Arp220	0.6253
141	10:51:53.78	+56:50:05.7	1.976	12.35 ± 0.89	–	–	1.0
142	10:51:58.53	+59:06:52.1	1.814	24.47 ± 0.86	–	Arp220	0.2643
145	10:52:59.88	+59:22:34.0	1.703	21.36 ± 1.04	–	Arp220	0.3807
146	10:53:08.25	+59:05:22.2	0.43	10.85 ± 1.36	–	–	0.4909
152	10:54:04.11	+57:40:19.8	1.101	18.23 ± 0.95	436.6 ± 4.53	Arp220	0.5371
157	10:54:47.29	+58:19:09.5	1.654	19.44 ± 0.95	–	Arp220	0.5587
162	10:55:49.88	+58:26:01.5	1.526	8.989 ± 0.75	–	Arp220	0.5942
165	10:56:39.42	+57:57:21.5	0.453	13.31 ± 1.02	–	Arp220	0.4404
168	10:57:05.41	+58:04:37.5	0.14	113.4 ± 1.25	211.53 ± 5.52	Arp220	0.4732
171	10:57:17.33	+58:01:03.0	3.311	12.35 ± 0.82	–	–	1.0
174	10:59:02.04	+58:08:48.7	2.244	16.07 ± 0.95	–	–	1.0
176	10:59:59.93	+57:48:48.2	0.453	25.07 ± 1.04	–	Arp220	0.7305
181	11:02:23.57	+57:44:36.3	0.226	24.95 ± 1.87	–	Arp220	0.7661
184	15:56:49.75	+54:35:51.3	1.71	8.880 ± 0.81	–	Arp220	0.5604
189	16:00:15.69	+55:23:00.0	0.673	13.80 ± 1.04	–	Arp220	0.7853
191	16:01:28.54	+54:45:21.4	0.728	37.92 ± 1.25	–	Arp220	0.7439
193	16:02:30.04	+54:36:58.5	1.327	9.020 ± 1.04	–	Arp220	0.674
195	16:02:50.97	+54:50:57.9	1.197	20.87 ± 1.09	–	Arp220	0.3485
200	16:05:23.11	+54:56:13.4	0.572	21.00 ± 1.11	–	Arp220	0.6389
204	16:06:37.88	+53:50:08.4	2.943	14.64 ± 0.99	–	–	1.0
205	16:06:55.36	+53:40:16.8	0.214	45.72 ± 1.99	50.85 ± 4.63	Arp220	0.5948
206	16:07:05.17	+53:35:58.6	3.653	22.2 ± 0.8	–	–	1.0
210	16:09:13.19	+53:54:29.6	0.992	12.23 ± 0.85	–	Arp220	0.6318
211	16:09:43.67	+53:30:41.0	1.328	28.92 ± 1.01	–	Arp220	0.441
212	16:09:50.72	+53:29:09.5	1.716	13.68 ± 1.14	–	Arp220	0.5853
213	16:09:53.03	+53:34:43.9	1.212	21.36 ± 0.94	–	Arp220	0.6154
214	16:10:07.12	+53:58:14.1	2.03	10.53 ± 1.21	–	–	1.0
217	16:12:38.28	+53:22:55.1	2.138	17.28 ± 1.36	–	–	1.0
218	16:12:57.60	+52:48:32.9	1.214	13.31 ± 1.38	–	Arp220	0.5722
221	16:30:31.47	+41:01:45.8	0.531	11.35 ± 1.03	–	Arp220	0.6577
225	16:31:28.60	+40:45:36.0	0.181	71.40 ± 1.62	–	Arp220	0.4198
226	16:31:35.47	+40:57:56.4	0.749	16.92 ± 0.77	–	Arp220	0.6203
227	16:31:43.76	+40:47:35.7	0.537	14.15 ± 1.37	–	Arp220	0.6927
232	16:32:25.56	+41:18:52.6	0.909	12.47 ± 1.07	–	Arp220	0.7071
235	16:33:08.29	+40:33:21.4	0.404	30.47 ± 0.97	103.18 ± 4.183	Arp220	0.396
238	16:33:52.34	+40:21:15.6	0.782	11.72 ± 1.1	–	Arp220	0.6571
240	16:34:26.28	+41:52:15.5	0.516	19.44 ± 1.6	–	Arp220	0.7376
244	16:35:31.06	+41:00:27.4	1.152	15.23 ± 1.09	–	Arp220	0.3848
246	16:36:18.51	+41:50:58.9	1.179	20.87 ± 1.0	–	Arp220	0.3819
247	16:36:31.29	+42:02:42.5	0.061	53.63 ± 1.37	91.19 ± 6.05	Arp220	0.7652

Table 4 – *continued*

Sequence number	RA	Dec.	z	S_{70} (mJy)	S_{160} (mJy)	SB	AGN_{frac}
250	16:37:09.32	+41:40:30.8	0.76	22.55 ± 0.93	–	Arp220	0.8411
251	16:37:14.40	+41:57:02.1	1.665	8.930 ± 1.03	–	Arp220	0.3886
253	16:37:26.89	+40:44:32.9	0.857	13.56 ± 0.94	–	Arp220	0.6531
255	16:37:59.16	+42:03:36.8	1.384	14.15 ± 1.02	–	Arp220	0.2503
265	16:40:18.34	+40:58:13.1	1.316	10.76 ± 0.85	–	Arp220	0.7006
267	16:40:39.31	+40:31:35.1	2.136	17.04 ± 1.32	–	–	1.0
273	16:43:11.84	+40:50:43.3	0.834	15.11 ± 1.01	–	Arp220	0.5112
276	16:43:43.25	+40:56:54.4	0.344	12.11 ± 1.37	–	Arp220	0.6623

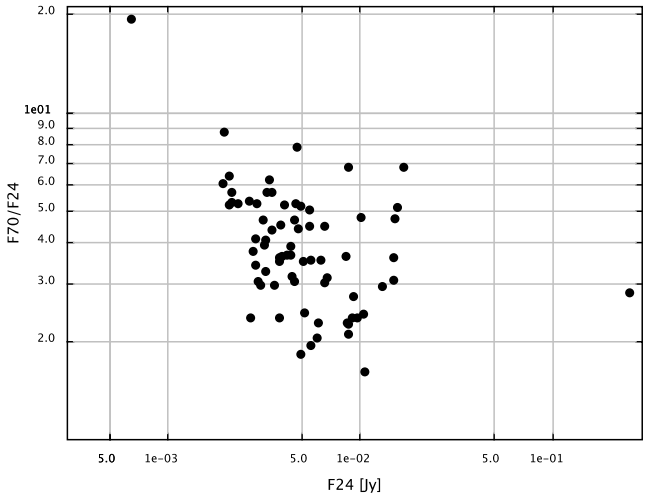

Figure 8. Observed F_{70}/F_{24} versus 24-μm flux for the 70 objects with 70-μm detections.

given parameter corresponding to the best-fitting model, are larger than 50 per cent. In order to understand this behaviour, one has to take into account the influence of each of the model parameters to the global model SEDs as well as the fact that not all parameters are independent. In fact, most of them are correlated in some way. For instance, the LoS and CF are tightly related: if the CF is small, LoS can vary in a larger interval; however as the CF increases, the LoS is restricted in those angles that permit direct view of the central source, especially in the case of high optical depths.

In fact, the parameters that are best constrained are L_{acc} and therefore R_{in} (from equation 3) and L_{IR}, despite the lack of points longward $\lambda = 24\,\mu m$. Fig. 13 shows how the fraction of objects with standard deviation of the luminosity over the best-fitting luminosity, $\sigma(L)/L(0)$, of $\leqslant$10 per cent (plain lines), $\leqslant$20 per cent (dashed lines), and $\leqslant$50 per cent (dotted lines), varies as a function of the first n solutions (n ranges from 2 to 30). L_{acc} is shown in black while L_{IR} is represented in red.

6 DISCUSSION

In this work, we compare observed and model SEDs of SDSS quasars with SWIRE counterparts aiming at constraining the model parameters and at quantifying the IR properties of bright quasars. The need for such an approach, though evident, was also stressed by Gallagher et al. (2007), who studied a sample of 234 SDSS quasars, most of which also belong to our sample, trying to quantify the effects of the luminosity on the shape of their SEDs in the mid-IR. Their conclusions were solely based on the observed SEDs and claimed that comparison with models would constrain physical parameters, many of which are dealt with in the present study.

We use a torus model with smooth dust distribution, originally presented in Fritz et al. (2006), even though there are conflicting suggestions in the literature as to whether tori could be smooth or clumpy. Smooth models have been tested on a variety of objects (e.g. Granato & Danese 1994; Fritz et al. 2006) yielding very good results. There is, however, evidence that clumpy tori might be more realistic (e.g. Risaliti, Elvis & Nicastro 2002); nevertheless, the few models in the literature were tested only on average SEDs (Nenkova et al. 2002) or on individual objects (Hönig et al. 2006) and only very recently on a sample of 21 obscured AGN (Polletta et al. 2008). Furthermore, Nenkova et al. (2002) explicitly addressed the issue of suppression of the 9.7-μm silicate feature, predicted in emission from smooth models, which was never till then supported observationally in type 1 objects, but the picture has changed since with *Spitzer* IRS observations of this feature in emission (Hao et al. 2005; Siebenmorgen et al. 2005; Sturm et al. 2005; Buchanan et al. 2006; Shi et al. 2006).

The issue of the influence of the accretion luminosity on the dust coverage is the source of an ongoing discussion in the literature. According to the receding torus paradigm (Lawrence 1991) the opening angle of the torus depends on the power of the central sources, with more powerful quasars sweeping larger amounts of dust leaving thus larger opening angles around them. In this approach, the Unified Scheme does not rely uniquely on the orientation of the dusty torus but on the dependence of the geometrical thickness and the optical depths on the central source. Evidence for receding tori is often found in studies of radio-loud AGN (e.g. Grimes, Rawlings & Willott 2003, 2005). Recently, Maiolino et al. (2007) presented results of a study of high luminosity quasars carried out with *Spitzer* IRS pointing towards decreasing CFs with increasing luminosity. In Section 5.2, we already suggested that the influence of L_{acc} on the torus geometry is demonstrated by the larger values of L_{acc} generaly occuring in objects with $\gamma = -6.0$. In fact, L_{acc} as derived from the best-fitting models also shows a slight dependence on CF with the average value of L_{acc} in bins of CF (red squares) decreases with increasing CF, as seen in Fig. 14. The dispersion on L_{acc} in each bin, however, is so large that the study is inconclusive.

The study of the sources with 70-μm detections, representing 25 per cent of the sample, suggested the presence of a strong starburst component in many of the cases. According to the best-fitting models and due to the flux limits of the sample, only objects with Arp220-like components were observed in 70 μm. One could argue that Arp220 is a heavily extinguished starburst, prototype ultraluminous IR galaxy in the local Universe and therefore unlikely to be found in high-redshift bright quasars. In a simpler approach, a blackbody of ∼30 K could have been used to account for the 70-μm detection but we used observed starburst templates instead, in the

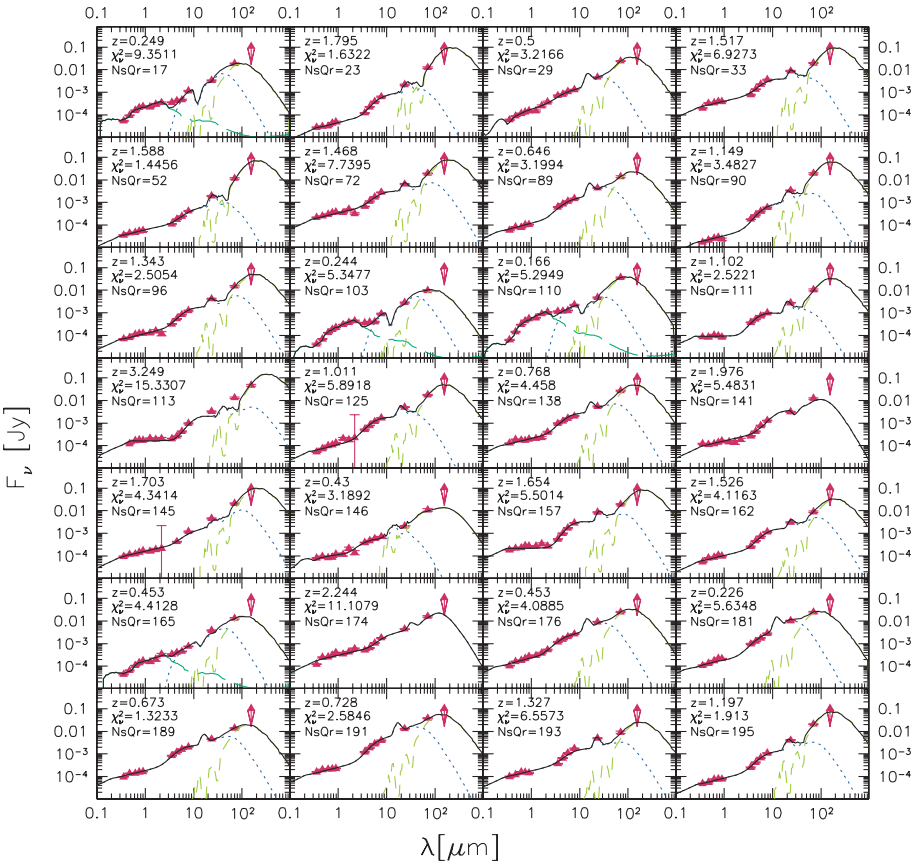

Figure 9. Observed (red triangles) and model (torus: blue dotted line; starburst: dashed light green; stars: long-dashed dark green) SEDs for the 55 objects with 70-μm detection and minimum $\chi^2 < 16$.

line of Fritz et al. (2006). However, we did exclude from the model grid models with $R_{\rm out}/R_{\rm in} = 300$, originally included in Fritz et al. (2006). These models imply larger dust distributions and lower dust temperatures and could have been used to reproduce the 70-μm detections. However, they would also correspond to tori with physical sizes of several hundred parsecs, sometimes even kpc, where star formation is likely to occur. Furthermore, at those distances the dust temperature would drop to temperatures typical of the dust of starburst or the diffuse dust responsible for cirrus emission.

One of the main points of this work is the use of tori models with low equatorial optical depths at 9.7μm, $\tau_{9.7} < 1.0$. Our study concludes that the presence of low optical depth tori around active nuclei is a possibility, and would imply only a minimum of modifications in the current picture of the Unified Scheme, namely the possibility of seeing type 1 objects while dust intercepts the LoS. A strong implication of this assumption would be the presence of the silicate feature at 9.7 μm in emission even in type 2 AGN. Such a feature was indeed observed recently in X-ray-selected type 2 AGN, using the *Spitzer* IRS (Sturm et al. 2006). The comparison between results yielded by all $\tau_{9.7}$ models and only high $\tau_{9.7}$ ones suggests a flattening of the distribution of the CF (see Fig. 4), increasing thus the apparent estimated ratio between type 2 and type 1 objects, as dust enshrouded AGN could still be seen as type 1 objects if seen through a low optical depth medium. In order to really probe the Unified Scheme and test the validity of the models, one would need to select a complete, volume-limited sample and study *all* AGN inside this volume, that is, of both types 1 and 2. The comparison of the tori model parameters and the AGN properties between the two types would prove or not the validity of the Unification Scheme, since the distribution of the various quantities should be the same for both types. Furthermore, the SED fitting could provide information about the orientation of the sources and finally the number of obscured versus unobscured quasars. This is the subject of our forthcoming work.

6.1 On the limitations of the models and results

It has been argued on many occasions that SED fitting techniques are both powerful *and* limited. Powerful because photometry is and will always be available for samples that are orders of magnitudes larger than spectroscopic ones; limited because it greatly depends on the quality of the photometric data, the model or synthetic SEDs used and the way of populating the multi-parameter space, the aliasing and degeneracy issues, and the priors one imposes. In the majority of cases, the value of SED fitting of large data sets is statistical, it helps define trends of the population under study as a whole, rather than the properties of individual objects, unless the sampling of their observed SEDs and the nature of the objects themselves allow for it.

Quasars in general have unmistakable signatures both in the UV/optical (in general blue continua attributed to the accretion on to the central black hole) and in the IR (IR bump due to dust torus emission). Furthermore, the sample under study has good wavelength coverage with SDSS, 2MASS and SWIRE data available, as detailed in Sections 2 and 5, helping to pin down the wavelength where the falling emission from the nucleus meets the rising emission from the dust (around 1 μm).

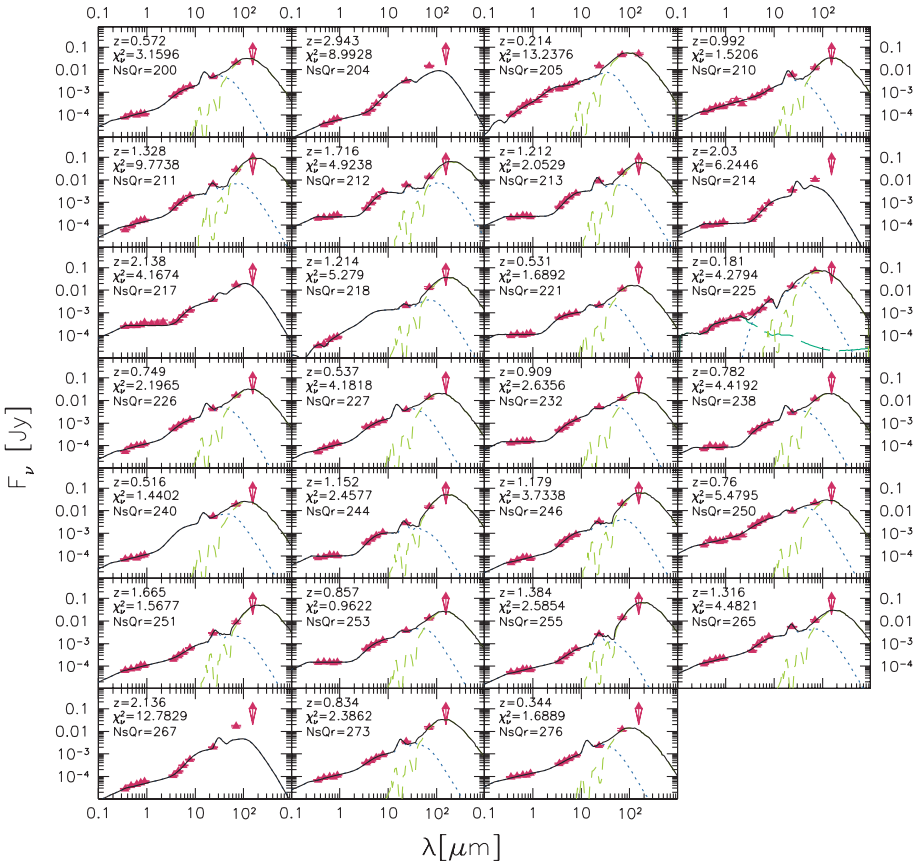

Figure 10. Same as in Fig. 9.

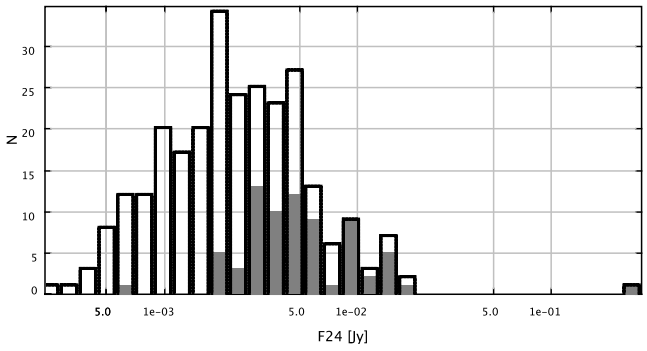

Figure 11. 24-μm flux histogram of the entire sample (open) and of the sources with 70-μm counterparts (greyed).

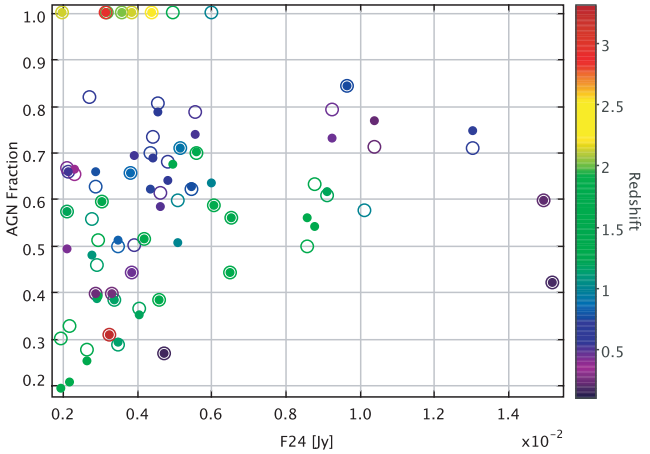

Figure 12. The fraction of IR luminosity, as defined in Section 4.1, attributed to the AGN as a function of their 24-μm flux and redshift, for the 55 objects with 70-μm detections and $\chi^2 < 16$. The filled (open) circles correspond to the run with all (high) $\tau_{9.7}$.

Since we are working with a pre-constructed grid of models, all of the model input parameters take discrete values and, in some cases, the model parameter space is sparsely populated. This is the case, for instance, of the assumed $R_{\rm out}/R_{\rm in}$ ratios, taking two discrete values of 30 or 100, or the angular variation of the dust density (factor γ in equation 1), being either 0.0 or −6.0. Recalculating a model to match each individual object would probably yield better results; however, this is computationally very demanding and sometimes even impossible, as some of the model parameters combination (very high optical depth, $\tau_{9.7} > 6.0$ and steep density profiles) would lead to a non-convergence of the torus model (see Fritz et al. 2006). This, of course, limits the accuracy of the results and therefore the values of the physical parameters derived should be seen as indicative.

ACKNOWLEDGMENTS

This work is based on observations made with the *Spitzer Space Telescope*, which is operated by the Jet Propulsion Laboratory, California Institute of Technology under NASA contract 1407. Support for this work, part of the Spitzer Space Telescope Legacy Science Program, was provided by NASA through an award issued by the

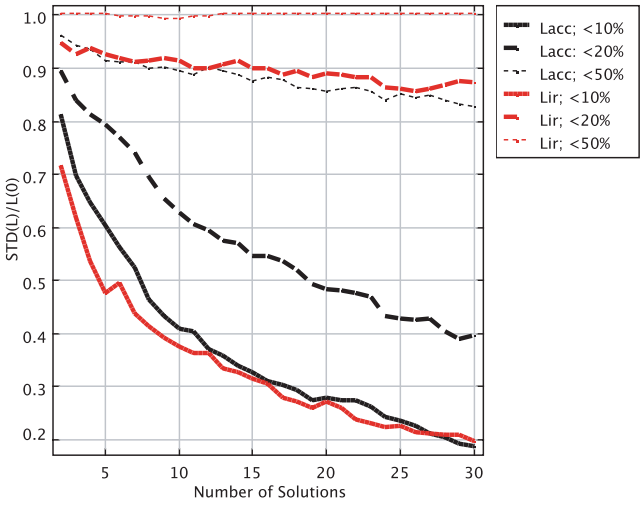

Figure 13. Percentage of objects with $\sigma(L)/L(0)$ below given thresholds, as function of the number of solutions. Black lines: $L_{\rm acc}$; red lines: $L_{\rm IR}$. The full, dashed and dotted lines represent the following thresholds: $\sigma(L)/L(0)$ of $\leqslant$10, 20 and 50 per cent, respectively.

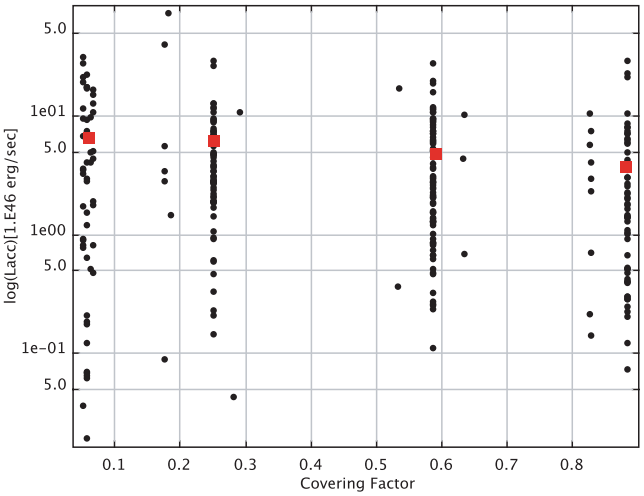

Figure 14. Accretion luminosity, $L_{\rm acc}$, versus CF: the mean $L_{\rm acc}$ (red squares) decreases in the bins with increasing CF but with large dispersions on the values of $L_{\rm acc}$.

Jet Propulsion Laboratory, California Institute of Technology under NASA contract 1407.

Funding for the creation and distribution of the SDSS Archive has been provided by the Alfred P. Sloan Foundation, the Participating Institutions, the National Aeronautics and Space Administration, the National Science Foundation, the US Department of Energy, the Japanese Monbukagakusho, and the Max Planck Society. The SDSS Web site is http://www.sdss.org/.

This publication makes use of data products from the 2MASS, which is a joint project of the University of Massachusetts and the Infrared Processing and Analysis Centre/California Institute of Technology, funded by the National Aeronautics and Space Administration and the National Science Foundation.

This work was supported in part by the Spanish Ministerio de Educación y Ciencia (Grants ESP2004-06870-C02-01 and ESP2007-65812-C02-02).

This work makes extensive use of TOPCAT (http://www.starlink.ac.uk/topcat/) a Virtual Observatory tool developed by M. Taylor.

REFERENCES

Adelman-McCarthy J. et al., 2006, ApJS, 162, 38
Babbedge T. et al., 2004, MNRAS, 353, 654
Barvainis R., 1987, ApJ, 320, 537
Beichman C. A., Cutri R., Jarrett T., Stiening R., Skrutskie M., 2003, AJ, 125, 2521
Bertelli G., Bressan A., Chiosi C., Fagotto F., Nasi E., 1994, AAPS, 106, 275
Bolzonella M., Miralles J.-M., Pelló R., 2000, A&A, 363, 476
Bressan A., Granato G. L., Silva L., 1998, AAP, 332, 135
Buchanan C. L., Gallimore J. F., O'Dea C. P., Baum S. A., Axon D. J., Robinson A., Elitzur M., Elvis M., 2006, AJ, 132, 401
Dullemond C. P., van Bemmel I. M., 2005, A&A, 436, 47
Efstathiou A., Rowan-Robinson M., 1995, MNRAS, 273, 649
Elitzur M., Shlosman I., 2006, ApJ, 648, L101
Fritz J., Franceschini A., Hatziminaoglou E., 2006, MNRAS, 366, 767
Gallagher S. C., Richards G. T., Lacy M., Hines D. C., Elitzur M., Storrie-Lombardi L. J., 2007, ApJ, 661, 30
Granato G. L., Danese L., 1994, MNRAS, 268, 235
Grimes J. A., Rawlings S., Willott C. J., 2003, New Astron. Rev., 47, 205
Grimes J. A., Rawlings S., Willott C. J., 2005, MNRAS, 359, 1345
Hao L. et al., 2005, ApJ, 625, L75
Hatziminaoglou E. et al., 2005, AJ, 129, 1198
Hönig S. F., Beckert T., Ohnaka K., Weigelt G., 2006, A&A, 452, 459
Jacoby G. H., Hunter D. A., Christian C. A., 1984, ApJS, 56, 257
Jaffe W. et al., 2004, Nature, 429, L47
Kaspi S., Smith P. S., Netzer H., Maoz D., Januzzi B. T., Giveon U., 2000, ApJ, 533, 631
Krolik J. H., Begelman M. C., 1988, ApJ, 329, 702
Laor A., Draine B. T., 1993, ApJ, 402, 441
Lawrence A., 1991, MNRAS, 252, 586
Lonsdale C. et al., 2003, PASP, 115, 897
Lonsdale C. et al., 2004, ApJS, 154, 54
McLure R., Jarvis M. J., 2002, MNRAS, 337, 109
McLure R., Dunlop J. S., 2004, MNRAS, 352, 1390
Maiolino R., Shemmer O., Imanishi M., Netzer H., Oliva E., Lutz D., Sturm E., 2007, A&A, 468, 979
Manske V., Henning T., Men'shchikov A. B., 1998, A&A, 331, 52
Mathis J. S., Rumpl W., Nordsieck K. H., 1997, ApJ, 217, 425
Nenkova M., Ivezic Z., Elitzur M., 2002, ApJ, 570, 9
Pier E. A., Krolik J. H., 1992, ApJ, 401, 99
Polletta M., Weedman D., Hoenig S., Lonsdale C. J., Smith H. E., Houck J., 2008, ApJ, 675, 960
Rees M., Silk J., Warner M. W., Wickramasinghe N. C., 1969, Nat, 223, 788
Richards G. T. et al., 2006, ApJS, 166, 470
Risaliti G., Elvis M., Nicastro F., 2002, ApJ, 571, 234
Rowan-Robinson M., 1992, MNRAS, 258, 787
Schartmann M., Meisenheimer K., Camenzind M., Wolf S., Henning Th., 2005, A&A, 437, 861
Shi Y. et al., 2006, ApJ, 653, 127
Shupe D. L. et al., 2008, AJ, 135, 1050
Siebenmorgen R., Haas M., Krügel E., Schulz B., 2005, A&A, 436, L5
Sturm E. et al., 2005, ApJ, 629, L21
Sturm E., Hasinger G., Lehmann I., Mainieri V., Genzel R., Lehnert M. D., Lutz D., Tacconi L. J., 2006, ApJ, 642, 81
Suganuma M. et al., 2006, ApJ, 639, 46
Surace J. A. et al., 2004, 'SWIRE ELAIS N1 Source Catalogs', http://adsabs.harvard.edu/abs/2004yCat.2255. . ..0S
van Bemmel T. M., Dullemond C. P., 2003, A&A, 404, 1

This paper has been typeset from a TEX/LATEX file prepared by the author.